15 Mar 2022

A Neural Network-Based Multivariate Seismic Classifier for Simultaneous Post-Earthquake Fragility Estimation and Damage Classification

Xinzhe Yuan

Genda Chen
Missouri University of Science and Technology, gchen@mst.edu

Pu Jiao

Liujun Li
Missouri University of Science and Technology, llpwc@mst.edu

et. al. For a complete list of authors, see https://scholarsmine.mst.edu/civarc_enveng_facwork/2340

Recommended Citation

X. Yuan et al., "A Neural Network-Based Multivariate Seismic Classifier for Simultaneous Post-Earthquake Fragility Estimation and Damage Classification," *Engineering Structures*, vol. 255, article no. 113918, Elsevier, Mar 2022.
The definitive version is available at https://doi.org/10.1016/j.engstruct.2022.113918

Engineering Structures 255 (2022) 113918

Contents lists available at ScienceDirect

Engineering Structures

journal homepage: www.elsevier.com/locate/engstruct

A neural network-based multivariate seismic classifier for simultaneous post-earthquake fragility estimation and damage classification

Xinzhe Yuan [a], Genda Chen [a,*], Pu Jiao [a], Liujun Li [a], Jun Han [a,b], Haibin Zhang [a]

[a] Missouri University of Science and Technology, Center for Intelligent Infrastructure, 500 W. 16th St., 112 Engineering Research Laboratory, Rolla, MO 65401, USA
[b] Chongqing University, 83 Shabei St., Shapingba District, Chongqing 400045, China

ARTICLE INFO

Keywords:
Artificial neural networks
Seismic damage classification
Fragility estimation
Multivariate seismic classifier
Intensity measures

ABSTRACT

A scalar intensity measure (*IM*) could be insufficient to represent the earthquake intensity and variety in fragility estimation. Introducing multiple *IM*s to conventional regression of fragility functions can be computationally demanding and require priori assumptions of functional forms. In this study, multivariate seismic classifiers with multiple *IM*s as inputs are developed based on artificial neural networks (*ANN*s) to address the above disadvantages of traditional regression approaches. Case studies of a four-story code-conforming benchmark building indicate that fragility estimates from multi-*IM ANN* classifiers lead to higher accuracy (5.0% to 7.7%) in system-level and element-level damage classification than the single-*IM* traditional fragility curves. Further studies of *IM* combinations show that the *ANN* performance can be improved by more *IM*s correlated with structural responses while compromised by redundant irrelevant *IM*s. The optimal *IM* set should be determined by correlation ranking and *ANN* predictive performance together. Moreover, the *ANN* configuration of the case-study building is optimized with five readily available *IM*s as inputs, which enable a near real-time (within 0.3 ms) prediction of future earthquake damage while maintain high predictive performance. Overall, the multivariate *ANN* seismic classifier can be a promising tool for simultaneous seismic fragility estimation and damage assessment.

1. Introduction

Seismic fragility analysis has been widely used in performance-based earthquake engineering. It mainly estimates the probabilities of a structure entering various limit states of interest as a function of a ground motion intensity measure (*IM*), which is often referred to as various smooth fragility curves based on a scalar *IM*. Mathematically, the fragility estimate can be defined as a probability of an engineering demand parameter D exceeding the structural capacity C, conditioned upon an *IM* through an approximate fragility function $p[D > C|IM]$. The accuracy of the traditional fragility curves largely depends on whether the selected *IM* sufficiently characterizes the earthquake record-to-record variation [1], because the earthquake variation has been widely demonstrated to be the primary uncertainty in seismic fragility analysis and damage evaluation [2–5]. Traditional smooth single-*IM* fragility curves were usually generated by the Cloud method [6], Incremental Dynamic Analysis (IDA) [7], Multiple Stripe Analysis (MSA) [8], and the improved approaches based on the former metamodels [9–12]. The Cloud method is introduced to illustrate the generation of traditional single-*IM* fragility curves. In the Cloud method, a seismic demand model needs to be built as shown in Equation (1),

$$\widehat{D} = aIM^b \text{ or } \ln\widehat{D} = b\bullet\ln\mathrm{IM} + \ln a \tag{1}$$

where $\widehat{D}$ is the median estimate of engineering demands in terms of *IM* with two regression parameters a and b. In the logarithmic space, $\ln D$ is assumed to follow a normal distribution with its median $\ln\widehat{D}$ given in Equation 1 and the standard deviation $\beta_{D|IM}$ estimated from Equation (2),

$$\beta_{D|IM} \cong \sqrt{\frac{\sum\left[(\ln d_i) - \ln\left(aIM_i^b\right)\right]^2}{N-2}} \tag{2}$$

where d_i and IM_i correspond to the engineering demand D and *IM* of the i^{th} ground motion record, and N is the total number of used ground motion records. The probability of D exceeding a certain demand d at a certain *IM* level is defined as Equation (3),

$$p[D \geq d|IM] = 1 - \Phi\left[\frac{\ln d - \ln\left(aIM^b\right)}{\beta_{D|IM}}\right] \tag{3}$$

where $\Phi[.]$ is normal distribution function. The median value $\widehat{C}$ of the

* Corresponding author.
E-mail address: gchen@mst.edu (G. Chen).

https://doi.org/10.1016/j.engstruct.2022.113918
Received 5 April 2021; Received in revised form 1 December 2021; Accepted 15 January 2022
Available online 3 February 2022

structural capacity C is also assumed to follow a lognormal distribution. Thus, in conjunction of these two lognormal distribution models, the probability of seismic demand D exceeding C at a certain IM level, i.e., the fragility estimate $p[D > C|IM]$, can be calculated by Equation (4),

$$p[D \geq C|IM] = \Phi\left[\frac{\ln(\widehat{D}/\widehat{C})}{\sqrt{\beta_{D|\mathrm{IM}}^2 + \beta_c^2}}\right] \tag{4}$$

where β_c is the lognormal standard deviation of C. Although the Cloud method is mainly based on statistical assumptions, it has been widely used due to its simplicity and reliability [13–16].

With the wide application of fragility function Equation (4), different improvements were proposed to enhance the fragility estimation. For example, robust fragility curves based on a single *IM* with a desired confidence interval were proposed to better consider the earthquake variation [12,17,18]. However, the uncertain fragility range instead of a determinate fragility value made it hard for the post-earthquake loss estimation and response decision making. On the other hand, vector-valued *IM*s with two or more elements were introduced based on the traditional regression approaches [19–23], to address the insufficiency of a scalar *IM* in fragility estimation. Du et al. [24] used stepwise regression methods based on the second order polynomial response surface model and second order polynomials to build the vector-*IM* seismic demand models for non-collapse and collapse states of the structures, respectively, to facilitate more accurate and reliable regional seismic risk estimates. However, introducing multiple *IM*s to conventional regression of fragility functions could be computationally demanding and require priori assumptions of functional forms (e.g., interactions between *IM*s). In the past two decades, multi-parameter *ANN*s have been widely used for the continuous estimation of seismic demands [25–31] to address the above disadvantages of conventional regression approaches. Fragility estimates based on these *ANN* continuous seismic demand models were demonstrated to be close to those of the traditional single-*IM* fragility curves. Recently, Kostinakis and Morfidis [32] and Morfidis and Kostinakis [33,34] used *ANN*s as a classifier to classify the earthquake-induced damage states of reinforced concrete (RC) buildings. In their studies, up to 14 *IM*s were selected as feature inputs of ground motion records and a significant conclusion was that *ANN*s could reliably and rapidly predict the damage states of RC buildings in real time after an earthquake. However, despite the successful application of *ANN*s in seismic damage classification, a simultaneous seismic fragility estimation is still absent, which is critical for the post-earthquake loss estimation.

To facilitate the simultaneous, direct end-to-end mapping of multiple *IM*s to not only the seismic damage classification but also the seismic fragility estimates, we develop the multivariate *ANN* seismic classifiers in this study. We first introduce the methodology of the multivariate *ANN* seismic classifiers, similar to the methodology in [32–34]. We then prepare training data based on the nonlinear time history analysis (*NLTHA*) of a code-conforming benchmark building. Next, a system-level *ANN* seismic classifier is trained to evaluate the global damage of the benchmark building. Different *IM* selections are used to train the system-level *ANN* classifier in order to shed some light on *IM* selection. The fragility estimates and damage classification of the system-level multi-*IM ANN* classifier are compared with those of the single-*IM* approaches. Furthermore, 72 element-level multi-*IM ANN* classifiers are trained to predict the local beam and column damage states. A damage map of beams and columns is generated by the 72 *ANN* classifiers and is validated by the map from *NLTHA* results. Similarly, different *IM* selections are used to train the element-level *ANN* classifiers to study the influence of *IM* selections on the *ANN* performance. For practical applications requiring computation-efficient training and deployment, a unified element-level *ANN* classifier is trained to predict the damage states of all elements instead of 72 individual classifiers. Both the system-level and element-level multi-*IM ANN* seismic classifiers of the benchmark building are retrained with five *IM*s that are readily available from the ShakeMap product by the United States Geological Survey (*USGS*) organization [35]. With these five readily available *IM*s, the multi-*IM ANN* seismic classifiers of a target structure can generate the fragility estimates and predict the resulting damage state of a future earthquake event in near real time. Finally, a few conclusions are drawn and future studies are directed.

2. Methodology of the multivariate *ANN* seismic classifier

A structure can be regarded as a classifier of ground motion records, which categorizes records to different resulting damage states of the structure. The classification function of a structure can be simulated by multivariate *ANN* seismic classifiers. Taking the system-level *ANN* classifier as an example, the classifier can be built by a three-layer perceptron shown in Fig. 1. The *ANN* input layer consists of an ensemble of selected *IM*s from the *IM* candidate pool listed in Table 1, which represents different characteristics of ground motion records like the intensity, duration, and frequency etc. Although flexible, two hidden layers with 20 hidden neurons in each layer are a good option to start with [36,37]. The output layer contains five output neurons corresponding to five damage states of the benchmark building: *None*, *Slight*, *Moderate*, *Extensive*, and *Complete* defined in HAZUS [38]. Neurons from layer to layer in the *ANN* classifier are fully connected by synaptic connections. Synaptic weights are assigned to these connections to form the weight matrices $W_{20,N+1}^{L_1}$, $W_{20,21}^{L_2}$, and $W_{5,21}^{L_3}$, as shown in Fig. 1. The activation functions $\sigma_1(\bullet)$ and $\sigma_2(\bullet)$ in the two hidden layers are rectified linear units (ReLU), given in Equation (5) [39], and the activation function $\sigma_3(\bullet)$ in the output layer is a softmax activation function defined by Equation (6) [40,41].

$$\sigma_1(s) = \sigma_2(s) = \begin{cases} 0 \ if \ s \leq 0 \\ s \ if \ s > 0 \end{cases} \tag{5}$$

$$\sigma_3(s) = \left\{\frac{e^{s_i}}{\sum_{k=1}^{J} e^{s_k}}\right\}, i = 1, 2, \cdots, J, \ J \text{ is the length of vector } s \tag{6}$$

Steps 1–4 represent the process of how the *IM*s of a ground motion record are fed forward in the *ANN* seismic classifier to generate the fragility estimates and damage classification. In **Step 1,** the vector $X = \{1, x_1, x_2, x_3, \cdots, x_N\}$ comprised of $N + 1$ elements is input to the *ANN* seismic classifier, where 1 is the bias item and $x_i, i = 1, 2, \cdots, N$ are the selected N *IM*s of the record. In **Step 2,** X is propagated into the hidden layer L_1 to output a new vector $a^{L_1} = W_{20,N+1}^{L_1} \cdot X^T$ (T means vector transposition). The elements of a^{L_1} will be fed into the 20 hidden neurons to pass through the activation function $\sigma_1(\bullet)$. Then, the new vector $Z^{L_1} = \{1, \sigma_1(a^{L_1})\}$ is produced by the L_1 hidden layer, as the input to hidden layer L_2. In **Step 3,** similar to **Step 2**, the output of L_2 plus the bias item forms $Z^{L_2} = \{1, \sigma_2(a^{L_2})\}$ as the input to output layer L_3, where $a^{L_2} = W_{20,21}^{L_2} \cdot {Z^{L_1}}^T$. In **Step 4,** a vector $a^{L_3} = W_{5,21}^{L_3} \cdot {Z^{L_2}}^T$ and its softmax activation function $Z^{L_3} = \sigma_3(a^{L_3})$ are calculated. Here, Z^{L_3} consists of five elements that represent the probability estimates of different damage states. Then, the damage state resulted from the ground motion record is categorized to the state that corresponds to the largest damage probability estimate. The arrow line on the top of Fig. 1 depicts the feedforward direction of the multiple *IM*s in the *ANN* seismic classifier to output fragility estimates and damage classification.

The performance of *ANN* seismic classifiers highly depends on the synaptic weights and the activation functions, which determine the information propagation in the *ANN* architecture. The activation function ReLU is selected for the two hidden layers due to its computational efficiency and convergence [42]. The softmax activation function is used in the output layer which has been widely used in *ANN* multi-classification tasks [43]. The optimal synaptic weights can be obtained through *ANN* training to achieve the best performance. Before training,

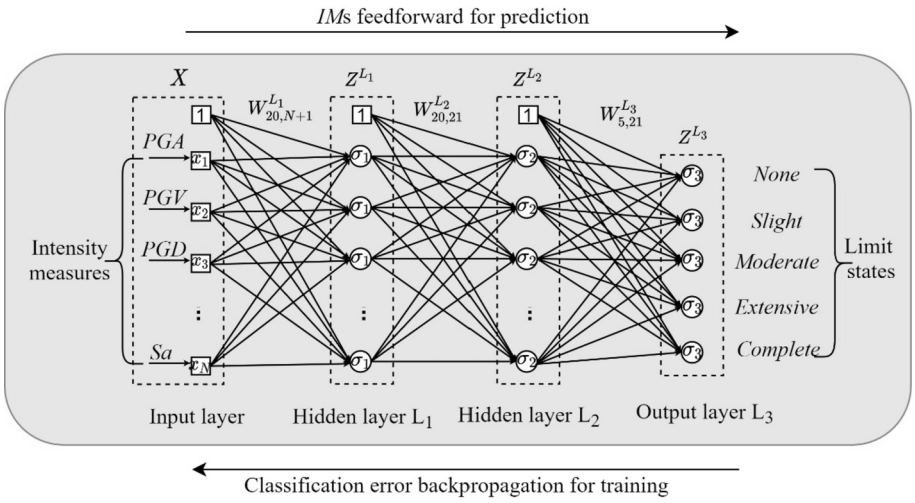

Fig. 1. The architecture of propsoed multivariate *ANN* seimic classifiers using multiple *IMs* as input and damage states resulted from ground motion records as output.

Table 1
Beam and column section properties.

	Beam				Column					
Section Tag	BS2	BS3	BS4	BS5	CS1	CS2	CS3	CS4	CS5	CS6
h (inch)	42	36	32	32	30	40	33	34	30	28
b (inch)	24	24	24	24	30	30	30	30	30	24
Long. Bar #	9	9	9	9	9	10	9	8	9	8
ρ_g (%)	1, top 0.8, bot	1, top 0.8, bot	0.9, top 0.6, bot	0.8, top 0.5, bot	2.7	1.8	2.4	1.2	1.8	1.6

a suite of ground motion records is collected as training samples. The resulting damage states to the structure by these records are obtained from *NLTHA* as the ground-truth states. Then, the *IMs* of training samples are fed into the *ANN* classifier to predict the damage states. The *ANN* predicted damage states are compared with the ground-truth states to calculate the classification error. An error function of cross-entropy loss is used to calculate the classification error E [44], as defined in Equation (7),

$$E = -\sum_{k=1}^{J} y_k \ln\left(Z_k^{L_3}\right) \tag{7}$$

where y_k (0 or 1) is the label of the k^{th} damage state, and $Z_k^{L_3}$ is the output in **Step 4**, which is a function of input X and all learnable synaptic weights W ($W^{L_1}_{20,N+1}$, $W^{L_2}_{20,21}$, and $W^{L_3}_{5,21}$). Therefore, E is a function of input X and W. The classification error $E(X, W)$ is backpropagated from the output layer to the first hidden layer through the gradient $\frac{\partial E(X,W)}{\partial W}$ via the gradient Chain rule. During the backpropagation, the learnable weights will be updated by Equation (8),

$$W^{new} = W^{old} - \eta \frac{\partial E(X, W)}{\partial W} \tag{8}$$

where η is a small positive value, known as the learning rate. Equation (8) is a basic gradient descent optimization algorithm. There are many more advanced optimization algorithms that can be found in the widely available literatures [45]. The training samples can be iteratively fed into the *ANN* classifier and in every iteration the learnable weights will be updated. When the best performance (usually lowest classification error on a separate test dataset) is achieved, the training process stops. To build the multivariate *ANN* seismic classifier for a target structure, the seismic responses and damage states of the structure under selected earthquake records are first obtained through *NLTHA*. Each record will then be labelled by its resulting damage state. Next, an *IM*-vector X of each record is calculated to characterize the record. *IM* vectors of many records are iteratively fed to the *ANN* seismic classifier until the classifier performs well on a separate test set of ground motion records. Finally, a well-trained *ANN* seismic classifier can be used to generate the seismic fragility estimates and damage evaluation of a future record based on its *IMs*.

3. Data preparation for multivariate *ANN* classifiers

3.1. The benchmark building

A representative, code-conforming RC benchmark building is selected to conduct the case study of the multivariate *ANN* seismic classifiers [46]. According to Haselton et al. [46], the four-story rectangular building of 4 × 6 bays resisted lateral loads through four moment-resisting frames around its perimeter, which was designed to comply with the 2003 International Building Code. The building was designed for the Los Angeles basin to represent a typical urban site in the high seismic region of California. Out of eight structural design options from A to H, Design A scheme is selected as the case-study structure. Table 1 shows the design information of its beams and columns. The perimeter frame of Design A is shown in Fig. 2(a). Fig. 2(b) represents the distributed-plasticity fiber element model [47]. Beams and columns are discretized into fibers and each fiber element has five integration points along its length. Nonlinear hysteretic characteristics of the element cross sections are captured by the uniaxial materials in OpenSEES [48], Concrete02 material model for unconfined and confined concrete (a nominal compressive strength 35 MPa), and Steel02 material model for reinforcement (a yield strength 460 MPa), respectively. Fig. 2 (c) shows the static pushover curves from [46] and this study, respectively. The lumped plastic hinges of an extra gravity frame caused a convergence problem in [46], which was addressed by gradually increasing the convergence tolerance and switching among multiple solution algorithms at each analysis step. Thus, the simulation time of

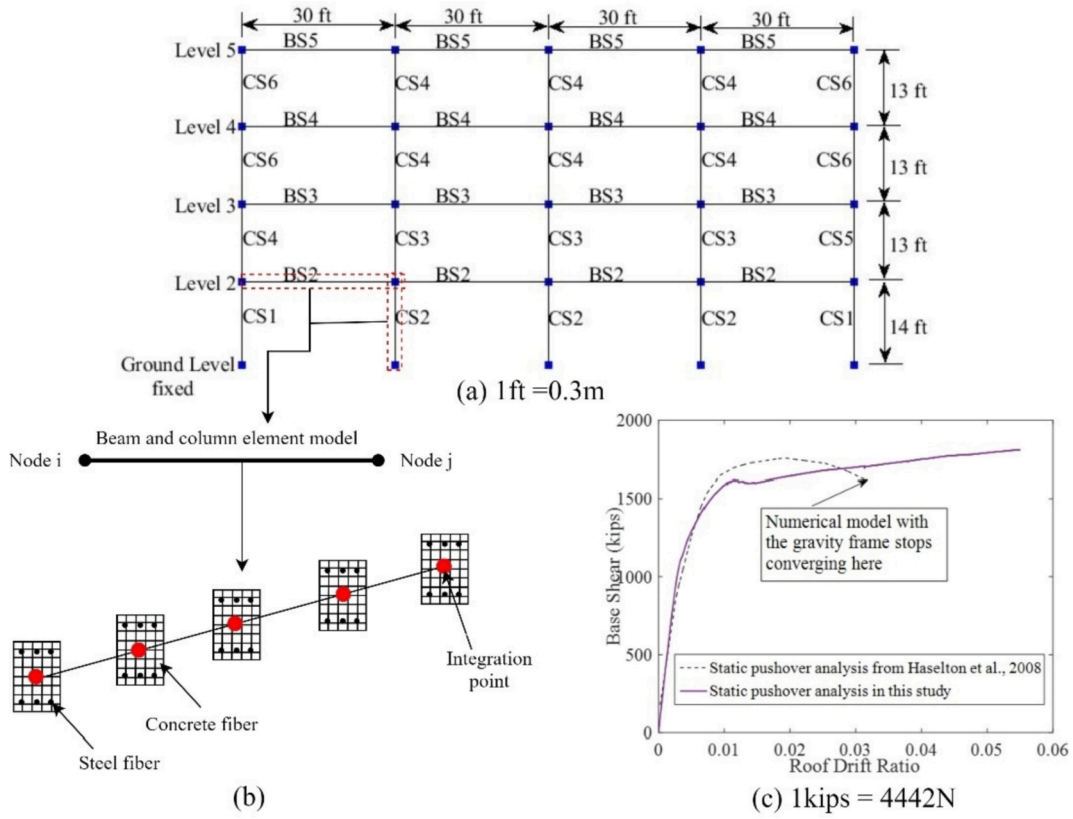

Fig. 2. Modeling and analysis of the perimeter frame: (a) elevation view of the frame; (b) illustration of the fiber distributed-plasticity element; (c) static pushover curves of Haselton et al. (2008) and this study.

more than 20,000 records would be significantly increased. Since the gravity frame was not typically considered to provide lateral resistance for the building [46], we only simulated the perimeter frame in this study to facilitate the *NLTHA*. A close pushover result to that of [46] was obtained as shown in Fig. 2(c), which validated our model only including the perimeter frame. Without the gravity frame, the perimeter-frame model converges under large deformations. Modal analysis shows that the fundamental period of the perimeter-frame model is 0.724 s (s for second), slightly shorter than 0.75 s of the original flexible-base model. Haselton et al. [46] also indicated that there was no statistically significant difference between the results of fixed-base and flexible-base models. Overall, the perimeter-frame model in this study can capture the structural properties of the benchmark building. Similar to the multi-*IM ANN* seismic demand model [31], we focus on the record-to-record uncertainty in this study and do not consider the material uncertainty which has been found to have very minimal influence on the seismic demand in previous studies [2–5,31]. Since only one RC building is used as the case-study structure, the structural geometry uncertainty is not considered in this study and recommended to be included in the input to *ANN* classifiers when many structures in the same class are studied.

As reported in [46], the peak drift ratio at collapse of the benchmark building would be in the order of 0.07–0.12. According to [38], for a RC moment-frame structure of 4–7 stories located in seismic active zones with most stringent seismic design requirements, like this selected office building in Los Angeles, the mean interstory drift threshold of *Slight* damage state is at 0.0033, *Moderate* at 0.0067, *Extensive* at 0.0200, and *Complete* at 0.0533. The threshold of *Complete* state conservatively includes the collapse range in [46]. These threshold values of HAZUS can lead to reasonable damage classification of the benchmark building based on the response range given in [46]. Therefore, a peak interstory $DR < 0.0033$ is defined as the damage state *None*, $0.0033 \leq DR < 0.0067$ as *Slight*, $0.0067 \leq DR < 0.02$ as *Moderate*, $0.02 \leq DR < 0.0533$ as *Extensive*, and $0.0533 \leq DR$ as *Complete*.

3.2. Ground motion records

A total of 1,993 ground motion records with their peak ground acceleration (*PGA*) larger than 1.47 m/s^2 are selected from the Pacific Earthquake Engineering Research Center (*PEER*) database (https://ngawest2.berkeley.edu/). Fig. 3 shows the locations of the selected earthquake events around the world, indicated by dots. The main consideration of this selection is to include a wide variety of records with different combinations of *IM* values. The preliminary *PGA* threshold is used mainly for the selection of strong ground motions such that enough severe damage states can be obtained. However, only 7 ground motion records of the original 1,993 records lead to *Complete* failure of the perimeter frame. In order to obtain enough *Complete*-state records in this study, one way to generate a large number of strong records is to scale up the historical ground motions [7] and realistic records could be obtained when the scaled records reach the target pseudo-spectral acceleration level at the fundamental period of the structure [49]. But excessive scaling can introduce bias to the numerical seismic response and a proper scaling limit is controversial.

According to [49], acceptable ground motion scaling limits varied widely from one (no scaling) to 10 or more in the engineering seismology community to limit excessive scaling of ground motion records. They found the scale-induced bias in seismic response also depended on the structural properties, intensity and considered dynamic responses, validated by other studies in [7,50]. Haselton et al. [46] scaled the ground motions up to 5 times in their study of the benchmark building, including near-fault ground motion records that are representative to the Los Angeles area. Since the main purpose of scaling is obtaining ample strong records of the *Complete* state instead of reaching a specific

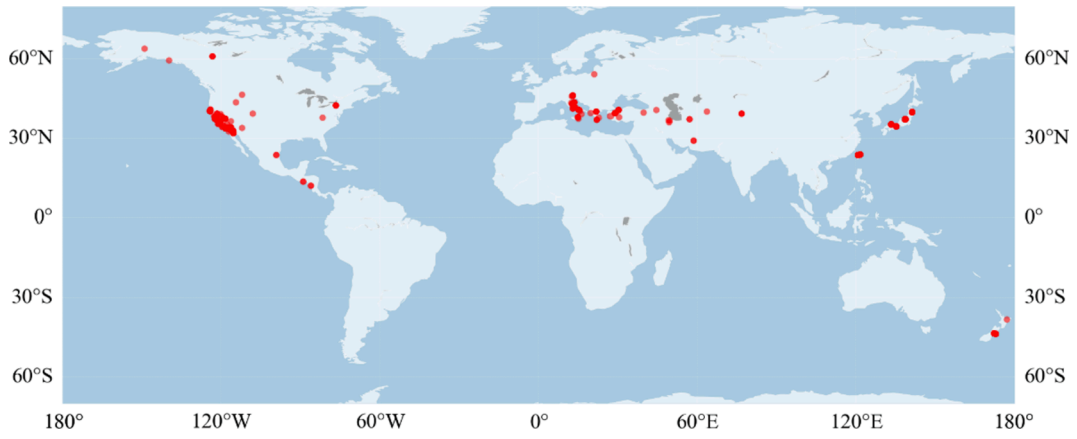

Fig. 3. Locations of selected earthquake events worldwide.

target pseudo-spectral acceleration level or fitting to a specific geographical area, the original 1,993 ground motion records are simply scaled by the acceptable limits of 2 to 10 times in amplitude with an increment of 1, which is a common way to obtain enough strong records in other studies [10,30,46,59–61]. The scaled ground motions amount to a pool of 19,930 training samples. In addition, 2,500 spectrum- and energy-compatible synthetic accelerograms from the original ground motion records are generated [54], to enrich the variety of training records. All together of the historical, scaled, and artificial records, 22,430 accelerograms are collected and are used to run the *NLTHA* of the benchmark building. To make sure that the scaled and artificial ground motions result in realistic seismic responses, we further screen the ground motion records based on their *DR* responses and exclude the records whose *DR*s are higher than 0.12 of the collapse range. The main reasons are that excessive *DR*s beyond the collapse range are unrealistic [46] and not suitable for building the traditional fragility curves in the later comparison to *ANN* classifiers. Therefore, they are excluded to guarantee fragility curves and *ANN* classifiers are compared by the same training and test datasets. A later examination of the excluded ground motions indicates that most of them are scaled with a factor over 8. The remaining 17,647 accelerograms were divided into five groups according to their *DR*s: 4,467, 3,249, 5,112, 3,953, and 866 ground motions labelled as *None*, *Slight*, *Moderate*, *Extensive,* and *Complete* state, respectively. Particularly, the 866 *Complete* ground motions are disaggregated into 327 and 511 records that result in the mechanism of first (37.8%) and third (59.0%) story, respectively, which are in general agreement with first (39%) and third (61%) story failure mechanism in [46]. To ensure the high performance of trained *ANN* ground motion classifiers, 866 records were randomly selected from each limit state (except for the *Complete* state) to form a balanced big dataset of 4,330 samples.

3.3. Intensity measures

*IM*s of the selected 4,330 ground motion records are calculated and used as input to the *ANN* seismic classifier. Many *IM*s have been proposed in the past to characterize a ground motion record. The correlation between different *IM*s and structural responses has been widely studied [1,35,55–61]. Since this study focuses on a direct mapping of multiple *IM*s to seismic fragility estimates and damage classification, for the sake of comprehensiveness, up to 50 *IM*s are selected from these previous studies to represent a ground motion record. As listed in Table 2, these 50 *IM*s are categorized into five groups related to the acceleration, velocity, displacement, duration, and frequency features of each ground motion, and are normalized to remove the effect of unit and scale differences [62] by Equation (9),

$$z = \frac{x - x_{min}}{x_{max} - x_{min}} \tag{9}$$

where x_{min} and x_{max} are the minimum and maximum values of each *IM*, and $z \in [0,1]$ is the normalized value of x. For consistency, the minimum and maximum values given in Table 2 follow the basic units: meter (m) for displacement and second (s) for time. The first four periods of the benchmark building in elastic range are $T_1 = 0.724\ s$, $T_2 = 0.247\ s$, $T_3 = 0.130\ s$, and $T_4 = 0.086\ s$. Only T_1/T_m was proposed to incorporate ground motion frequency contents in [59], where T_m represented the mean period of the ground motion. In this study, higher modes of the benchmark building are also included to potentially capture their contribution to the structural damage.

4. System-level multivariate *ANN* seismic classifier

4.1. Correlation ranking of selected IMs

Feature ranking and selection is essential to remove irrelevant information and improve the performance of predictive models, where the filter feature selection methods use statistical models to score the correlation between input and target variables, and features with high scores are regarded as important features [63]. Therefore, a correlation ranking between the 50 *IM*s and the seismic demand *DR* is studied first to provide a guideline for *IM* selection from the 50 *IM*s. Riddell [57] measured the correlation between an *IM* and several considered structural responses by measuring the regression fitness R^2 of Equation (1). Padgett et al. [1] used indicators like Efficiency ($\beta_{D|IM}$ of Equation (2)), Practicality (b of Equation (1)), and Proficiency ($\zeta = \beta_{D|IM}/b$) etc. to find the most correlated *IM* to seismic demands. Higher b and R^2, lower $\beta_{D|IM}$ and ζ mean higher correlation. We generate the $\beta_{D|IM}$, b, ζ, and R^2 for 10 *IM*s, as listed in Table 3. *EPA* and *Ih* are the two most important *IM*s as *EPA* has the highest b and lowest ζ, while *Ih* has the lowest $\beta_{D|IM}$ and highest R^2.

Since R^2 is usually used for *IM* selection in Cloud method, which will be compared to the *ANN* seismic classifiers later, we also use R^2 to roughly rank the 50 *IM*s for *IM* selection in *ANN* training, as shown in Fig. 4. Although the Cloud method typically uses unscaled historical ground motions, scaled records have also been used to obtain sufficient data points for Cloud method [10,31,51–53]. To study the influence of different *IM* selections to the *ANN* performance, the 50 *IM*s and their 10 subsets of various numbers (1, 6, 11, 16, 21, 26, 31, 36, 41, and 46) are selected in two groups. The first group is generated from the most important *Ih* to the least important *RDV*. For example, the subset with one *IM* is *Ih* only. The subset with six *IM*s consists of *Ih*, *CSA*, *EPA*, *PGV*, *Sa-1.0*, and *VC1*. The second group is generated from the least important *RDV* to the most important *Ih*.

Table 2
Definition of selected *IMs* and their minimum and maximum values.

Type	IMs	Definition	Notes	Max	Min
Acceleration-related *IMs*	*PGA*	$\max\left\|\ddot{u}_g(t)\right\|$	Peak ground acceleration.	242.2	1.47
	ASQ	$\int_0^{t_{tot}}\left[\ddot{u}_g(t)\right]^2 dt$	Squared acceleration, where t_{tot} is the total duration of a record.	1.6×10^{4}	0.11
	ARS	$\sqrt{\int_0^{t_{tot}}\left[\ddot{u}_g(t)\right]^2 dt}$	Root square of *ASQ*.	127.0	0.33
	Ia	$\frac{\pi}{2g}\int_0^{t_{tot}}\left[\ddot{u}_g(t)\right]^2 dt$	Arias intensity, where g is the gravitational acceleration.	2.6×10^{3}	0.02
	Arms	$\sqrt{\frac{1}{t_{tot}}\int_0^{t_{tot}}\left[\ddot{u}_g(t)\right]^2 dt}$	Root-mean-square acceleration.	16.7	0.02
	Ic	$\mathrm{Arms}^{1.5}*t_2{}^{0.5}$	Characteristic intensity, where t_2 is a duration-related *IM* below.	248.8	2.7×10^{-3}
	EPA	$\frac{1}{2.5}\int_{0.1}^{2.5} S_a(T,0.05)dT$	Effective peak acceleration from S_a	88.0	0.06
	SaTf1	$S_a(T_1,0.05)$	Spectral acceleration S_a at fundamental period T_1 of a structure with 5% damping.	132.9	0.02
	SaTf2	$S_a(T_2,0.05)$	Spectral acceleration S_a at second period T_2	601.5	0.26
	SaTf3	$S_a(T_3,0.05)$	Spectral acceleration S_a at third period T_3	319.0	1.03
	SaTf4	$S_a(T_4,0.05)$	Spectral acceleration S_a at fourth period T_4	365.6	1.34
	Sa-0.3	$S_a(T=0.3,0.05)$	Spectral acceleration S_a at 0.3 *s*	463.0	0.24
	Sa-1.0	$S_a(T=1.0,0.05)$	Spectral acceleration S_a at 1.0 *s*	113.6	0.01
	Sa-3.0	$S_a(T=3.0,0.05)$	Spectral acceleration S_a at 3.0 *s*	22.6	2.0×10^{-3}
	CSA	$S_a(T_1,0.05)\left(\frac{S_a(2T_1,0.05)}{S_a(T_1,0.05)}\right)^{0.5}$	Cordova spectral acceleration.	82.4	8.7×10^{-3}
	ASI	$\int_{0.1}^{0.5} S_a(T,0.05)dT$	Acceleration spectral intensity.	150.3	0.12
	CAV	$\int_0^{t_{tot}}\left\|\ddot{u}_g(t)\right\|dt$	Cumulative absolute velocity.	432.1	0.32
Velocity-related IMs	*PGV*	$\max\left\|\dot{u}_g(t)\right\|$	Peak ground velocity.	8.2	0.01
	VSQ	$\int_0^{t_{tot}}\left[\dot{u}_g(t)\right]^2 dt$	Squared velocity.	118.3	6.3×10^{-5}
	VRS	$\sqrt{\int_0^{t_{tot}}\left[\dot{u}_g(t)\right]^2 dt}$	Root-square velocity of *VSQ*.	10.9	0.01
	Vrms	$\sqrt{\frac{1}{t_{tot}}\int_0^{t_{tot}}\left[\dot{u}_g(t)\right]^2 dt}$	Root-mean-square velocity.	1.28	6.1×10^{-4}
	Ih	$\int_{0.1}^{2.5} PS_v(T,0.05)dT$	Intensity of pseudo-velocity spectrum PS_v	21.2	6.3×10^{-3}
	CAD	$\int_0^{t_{tot}}\left\|\dot{u}_g(t)\right\|dt$	Cumulative absolute displacement.	130.4	0.01
	SvTf1	$S_v(T_1,0.05)$	S_v at the fundamental period T_1 of a structure with 5% damping.	15.3	2.0×10^{-3}
	SvTf2	$S_v(T_2,0.05)$	S_v at the second period T_2	22.4	0.01
	SvTf3	$S_v(T_3,0.05)$	S_v at the third period T_3	5.7	0.02
	SvTf4	$S_v(T_4,0.05)$	S_v at the fourth period T_4	4.1	0.01
	VC1	$\mathrm{PGV}*t_2{}^{0.25}$	A compound index of *PGV* and t_2.	13.8	0.01
	VC2	$\mathrm{PGV}^{2/3}*t_2{}^{1/3}$	A compound index of *PGV* and t_2.	9.8	0.06
Displacement-related *IMs*	*PGD*	$\max\left\|u_g(t)\right\|$	Peak ground displacement.	58.7	2.3×10^{-4}
	DSQ	$\int_0^{t_{tot}}\left[u_g(t)\right]^2 dt$	Squared displacement.	4.3×10^{5}	1.4×10^{-8}
	DRS	$\sqrt{\int_0^{t_{tot}}\left[u_g(t)\right]^2 dt}$	Root-square displacement of *DSQ*.	659.1	1.2×10^{-4}

(*continued on next page*)

Table 2 (*continued*)

Type	IMs	Definition	Notes	Max	Min
	Drms	$\sqrt{\frac{1}{t_{tot}}\int_0^{t_{tot}}[u_g(t)]^2 dt}$	Root-mean-square displacement	38.0	3.3×10^{-5}
	CAI	$\int_0^{t_{tot}}\|u_g(t)\|dt$	Cumulative absolute intensity.	9.5×10^{3}	3.2×10^{-4}
	SdTf1	$S_d(T_1, 0.05)$	S_d at the fundamental period T_1 of a structure with 5% damping.	1.8	2.2×10^{-4}
	SdTf2	$S_d(T_2, 0.05)$	S_d at the second period T_2	0.83	3.6×10^{-4}
	SdTf3	$S_d(T_3, 0.05)$	S_d at the third period T_3	0.1	3.2×10^{-4}
	SdTf4	$S_d(T_4, 0.05)$	S_d at the fourth period T_4	0.05	1.7×10^{-4}
	DC	$PGD * t_2^{1/3}$	A compound index of *PGD* and t_2.	240.2	3.1×10^{-4}
Duration-related *IMs*	t_1	$t(0.75Ia)$-$t(0.05Ia)$	Time duration between 75% *Ia* and 5% *Ia*.	33.2	0.1
	t_2	$t(0.95Ia)$-$t(0.05Ia)$	Time duration between 95% *Ia* and 5% *Ia*.	216.1	0.33
	t_3	–	The time elapsed between the first and last excursions of acceleration above 0.02 *g*.	286.7	0.51
	t_4	–	The time elapsed between the first and last excursions of acceleration above 0.05 *g*.	275.5	0.12
Frequency-related *IMs*	*RVA*	*PGV/PGA*	A compound index of *PGA* and *PGV*.	0.9	7.5×10^{-3}
	RDV	*PGD/PGV*	A compound index of *PGV* and *PGD*.	41.1	0.01
	T_m	$T_m = \frac{\sum_i C_i^2 \times \frac{1}{f_i}}{\sum_i C_i^2}$	T_m is the mean period of ground motion. C_i is the Fourier amplitude at a frequency f_i.	2.4	0.06
	Tr_1	T_1/T_m	First period T_1 over T_m	12.1	0.31
	Tr_2	T_2/T_m	Second period T_2 over T_m	4.1	0.10
	Tr_3	T_3/T_m	Third period T_3 over T_m	2.2	0.06
	Tr_4	T_4/T_m	Fourth period T_4 over T_m	1.5	0.04

Table 3
$\beta_{D|IM}$, b, ζ, and R^2 of selected 10 *IMs*.

	IMs									
Parameters	*PGA*	*EPA*	*Sa-1.0*	*CSA*	*CAV*	*PGV*	*Ih*	*CAD*	*Sa-3.0*	*Sa-0.3*
b	1.082	**1.409**	1.079	1.125	1.061	1.380	1.242	0.808	0.833	1.067
$\beta_{D\|IM}$	1.094	0.602	0.621	0.586	0.962	0.616	**0.545**	0.929	0.835	1.018
ζ	1.011	**0.428**	0.575	0.521	0.906	0.446	0.439	1.149	1.003	0.954
R^2	0.412	0.822	0.811	0.831	0.546	0.814	**0.854**	0.576	0.657	0.491

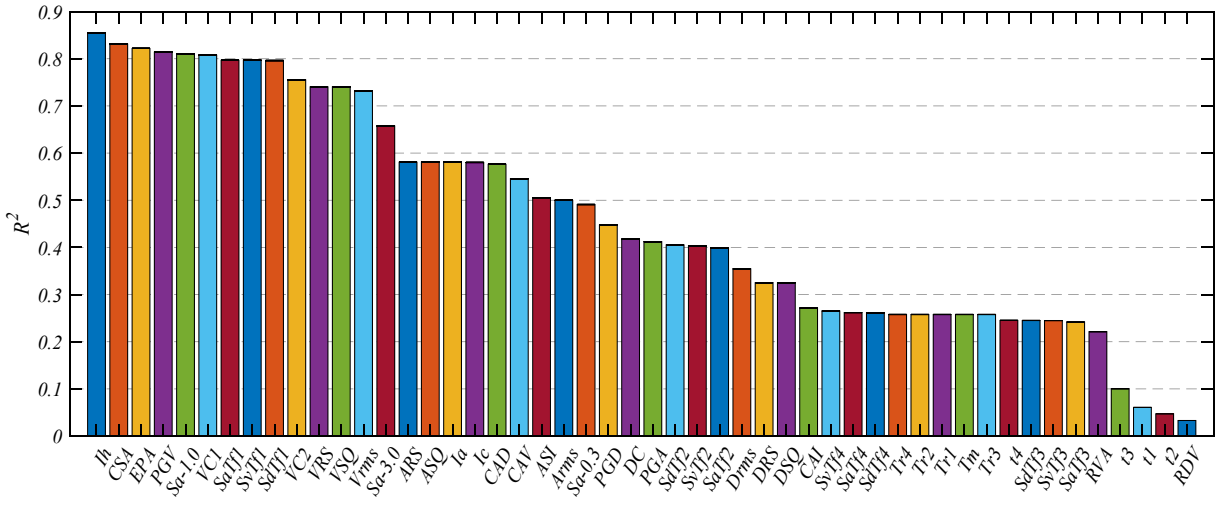

Fig. 4. Correlation ranking of the selected 50 *IMs* to the peak interstory *DR*.

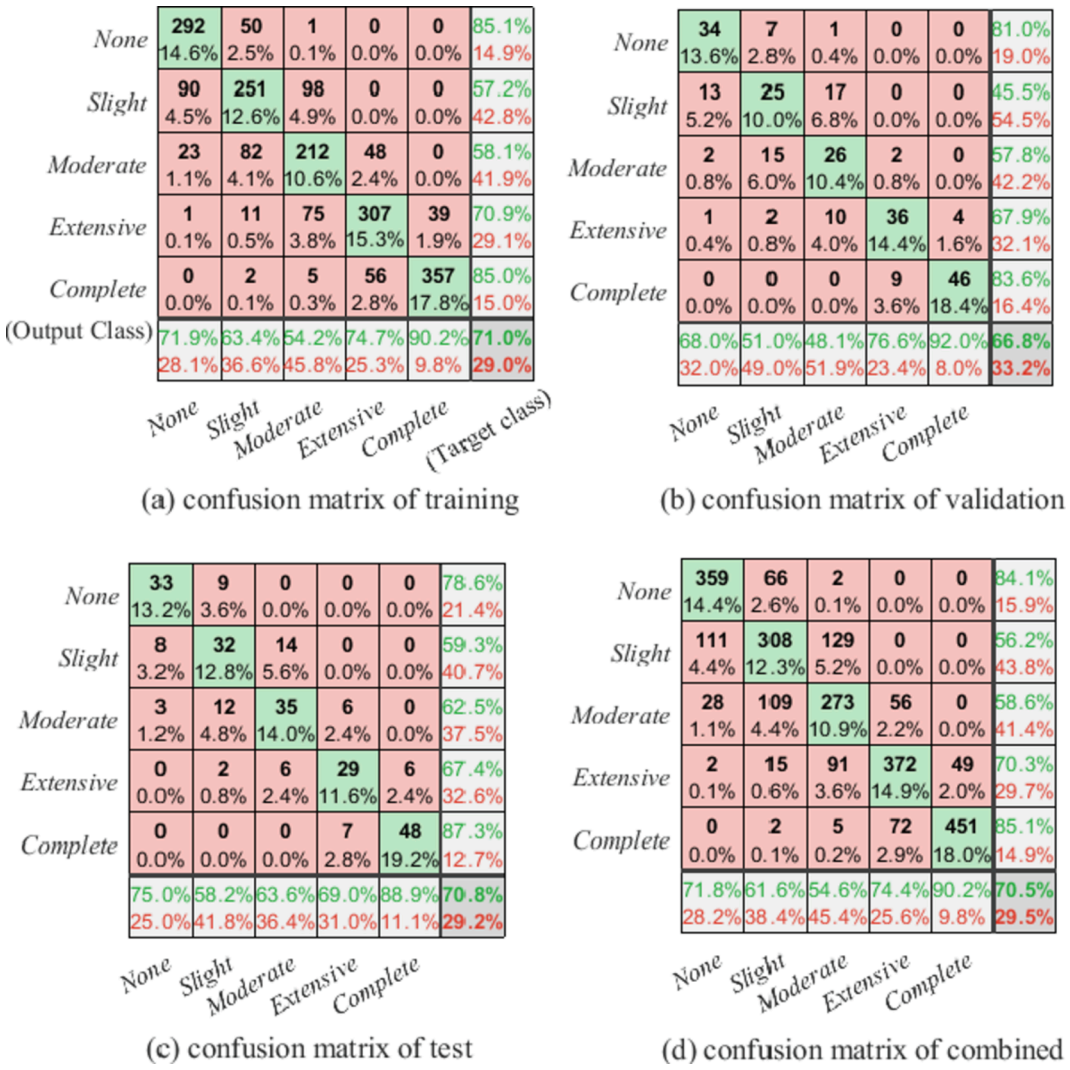

Fig. 5. Confusion matrices of the three susbets and the whole traning dataset where green and red cells are the percentages of right and wrong classifications in the current subset, respectively: (a) training subset; (b) validation susbset; (c) test subset; (d) whole dataset of the three combined subsets.

4.2. *ANN training*

The selected 4,330 records were divided into two datasets for training and test, respectively. The training dataset has 2,500 samples, 500 from each of the five damage states. The test dataset consists of 1,830 samples, 366 from each damage state. The holdout test dataset is not involved in the training process and mainly for the unbiased model test on unseen data. The output matrix for training is 2,500 × 5, where 2,500 is the number of training samples and 5 corresponds to the number of damage states. The input matrix for training is 2500 × *U*, where *U* represents the number of the *IMs* of a ground motion record. To fit in the built-in *ANN* training framework in MATLAB platform, the 2,500 training records are further divided into three subsets for training, validation, and test with ratios of 80%, 10%, and 10%. The training subset is iteratively fed to the *ANN* classifier to compute the gradient and update the weights, as defined in Equation (8). The validation subset is used to monitor the performance of the *ANN* performance. When the validation error starts to rise while the training error decreases, an overfitting problem appears and the training should stop to generate the best *ANN* performance. An overfitting *ANN* classifier will lose performance on unseen data like future ground motions. The test subset is also monitoring the model training. When a minimum test error is significantly different from the validation error, it indicates a poor division of the 2,500 training samples and a retraining of the *ANN* classifier should

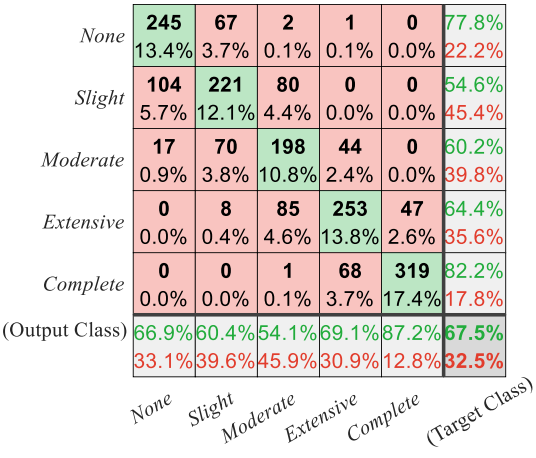

Fig. 6. Confusion matrix of the test dataset comprised of 1830 unseen records where green and red cells are the percentages of right and wrong classifications in the test dataset, respectively.

be considered. The scaled conjugate gradient (*SCG*) backpropagation algorithm is used in the *ANN* training [64]. Six key training parameters: *epochs*, *goal*, *time*, *lr*, *min_grad*, and *max_fail* are needed to control the training process. Here, *epochs* is the maximum number of epochs to train, where one training epoch means all samples in the training subset are used to train the *ANN* classifier once; *goal* is the expected performance goal; *lr* is the learning rate; *time* is the maximum time to train in seconds; *min_grad* is the minimum performance gradient; and *max_fail* is the maximum number of validation failures. In this study, *lr* is set as 0.01 and the training will be stopped when *epochs* = 1,000 or *goal* = 0 or *min_grad* = 10^{-6} or *max_fail* = 10, whichever arrives first. More details of the *ANN* training parameters can be found in [65]. After the *ANN* classifier has been trained, the test dataset of the remaining 1,830 samples will be used to understand its performance.

Fig. 5 shows the classification performance of the 50-*IM ANN* seismic classifier on the training dataset in the form of confusion matrices. A confusion matrix shows the classification result of each damage state by the *ANN* classifier. Taking Fig. 5(a) of the training subset as an example, rows of the confusion matrix show the prediction states (denoted as Output Class) of the 2,000 ground motion records. For instance, in the second row of *Slight* state, the *ANN* classifier predicts 439 (90 + 251 + 98) records as *Slight*-state ground motions including 188 (90 + 98) false positive cases. Indeed, 90 of the false *Slight* records belong to the *None* state while 98 belong to the *Moderate* state. The true positive ratio in the second row is 57.2%, known as the precision ratio p_r. On the other hand, columns of the confusion matrix in Fig. 5(a) show the true states (denoted as Target Class) of the 2,000 records. For instance, the second column shows that, among 396 (50 + 251 + 82 + 11 + 2) true *Slight*-state records, 251 records are correctly predicted by the *ANN* classifier while 145 records are misclassified as other damage states. The correct classification ratio in the second column is 63.4%, known as the recall ratio r_c. The overall classification accuracy of the 2,000 records is given in the lower right corner cell of the matrix as 71.0%, which is the ratio of the correctly classified records in the whole training subset. To comprehensively evaluate the performance of the *ANN* classifier, a compound index F-measure of p_r and r_c is used [66], which is defined as Equation (10),

$$\text{F-measure} = \left(1+\beta^2\right)\frac{p_r \bullet r_c}{\beta^2 \bullet p_r + r_c} \tag{10}$$

where β is an importance weighting factor on r_c over p_r. In the seismic-induced damage classification task, p_r and r_c are deemed equally important because most true samples should be identified in each damage state without raising too many false alarms. Thus, β is equal to 1. A higher F-measure of a damage state, closer to 1, indicates better performance of the *ANN* classifier for that particular damage state while a higher overall accuracy closer to 1 means better performance of the *ANN* classifier for all damage states. In this study, we use the F-measure and the overall accuracy to evaluate the performance of the *ANN* seismic classifier. Fig. 5 shows that the overall accuracies of the three subsets and combined training dataset are not significantly different from each other, meaning no overfitting of this *ANN* classifier. Fig. 6 shows the confusion matrix of the test dataset, which is comprised of the 1,830 test ground motions. These ground motion records are not involved in the previous training and are regarded as unseen future records. The confusion matrix shows that the *ANN* seismic classifier has an overall prediction accuracy of 67.5% on the test dataset.

Fig. 7 depicts the F-measure for each of the five damage states and the overall accuracy against different *IM* subsets previously generated by the correlation ranking in Fig. 4. It can be seen from Fig. 7(a) that the *ANN* prediction performance changes very slightly with the additional *IM*s as long as the most correlated *IM* is included. Specifically, the *ANN* classifier trained with the single top-ranking *Ih* achieves 65.4% overall accuracy, then the highest 68.9% with 36 *IM*s, and 67.5% with 50 *IM*s as inputs. The increase of the overall accuracy at a single optimal *IM* to 36 *IM*s is not significant but cannot be considered as negligible, indicating that it is beneficial to combine more *IM*s with the optimal *IM* for damage classification. On the other hand, the decrease of the overall accuracy from 36 *IM*s to 50 *IM*s shows that extraneous or irrelevant *IM*s might compromise the *ANN* performance. The optimal number of *IM*s should be selected based on correlation ranking and model performance together. Fig. 7(b) shows that the *ANN* prediction performance only achieves an overall accuracy of 29.5% with the least correlated *IM RDV*, 54.3% with 6 *IM*s, and the highest 67.5% with 50 *IM*s. The remarkable growth of the overall accuracy from a lowest-ranking *IM* to 6 *IM*s reveals a practical benefit of using multiple *IM*s, that is, when higher-ranking *IM*s are unknown or hard to access, a group of less correlated *IM*s can generate comparable classification performance to that of the most correlated *IM*, enabling more flexibility of *IM* selection in seismic fragility estimation and damage classification. It is also noticed in Fig. 7 (b) that the overall accuracy tends to be steady after 6 *IM*s, indicating it is less beneficial to add more *IM*s after a certain amount. In contrary, redundancy of *IM*s can compromise the *ANN* performance, e.g., *41* IMs in Fig. 7(b). This phenomenon is also observed in Fig. 8 and 11(b). Overall, Fig. 7 validates the correlation ranking of *IM*s in Fig. 4 and shows that multiple *IM*s can improve the performance of *ANN* seismic classifiers. However, the optimal number of *IM*s should be determined by correlation ranking and model performance together to remove the

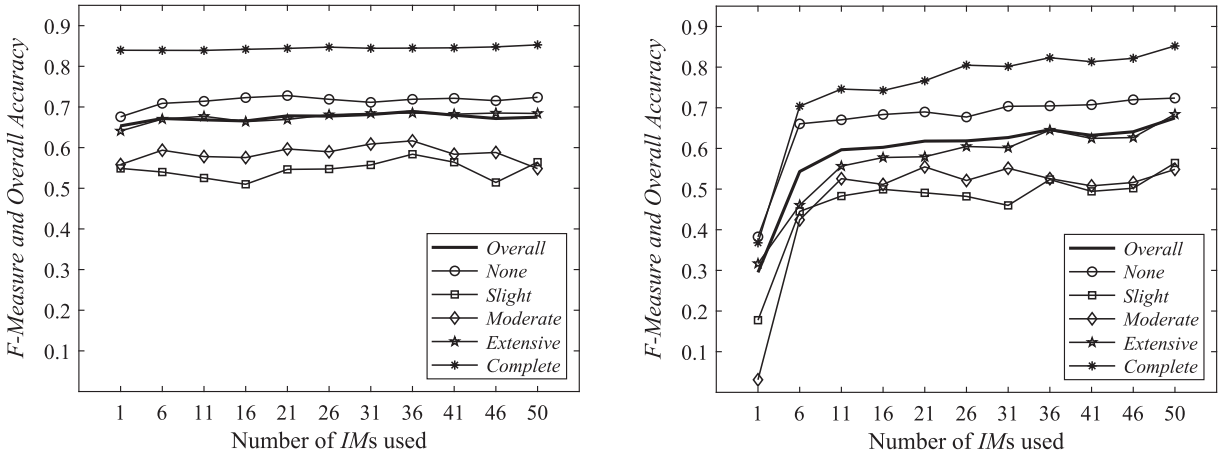

(a) *IM* subsets from most to least correlated (b) *IM* subsets from least to most corelated

Fig. 7. System-level *ANN* classification performance based on different subsets of *IM*s: (a) *IM* subsets selected in the most to least correlation order; (b) *IM* subsets selected in the least to most correlation order.

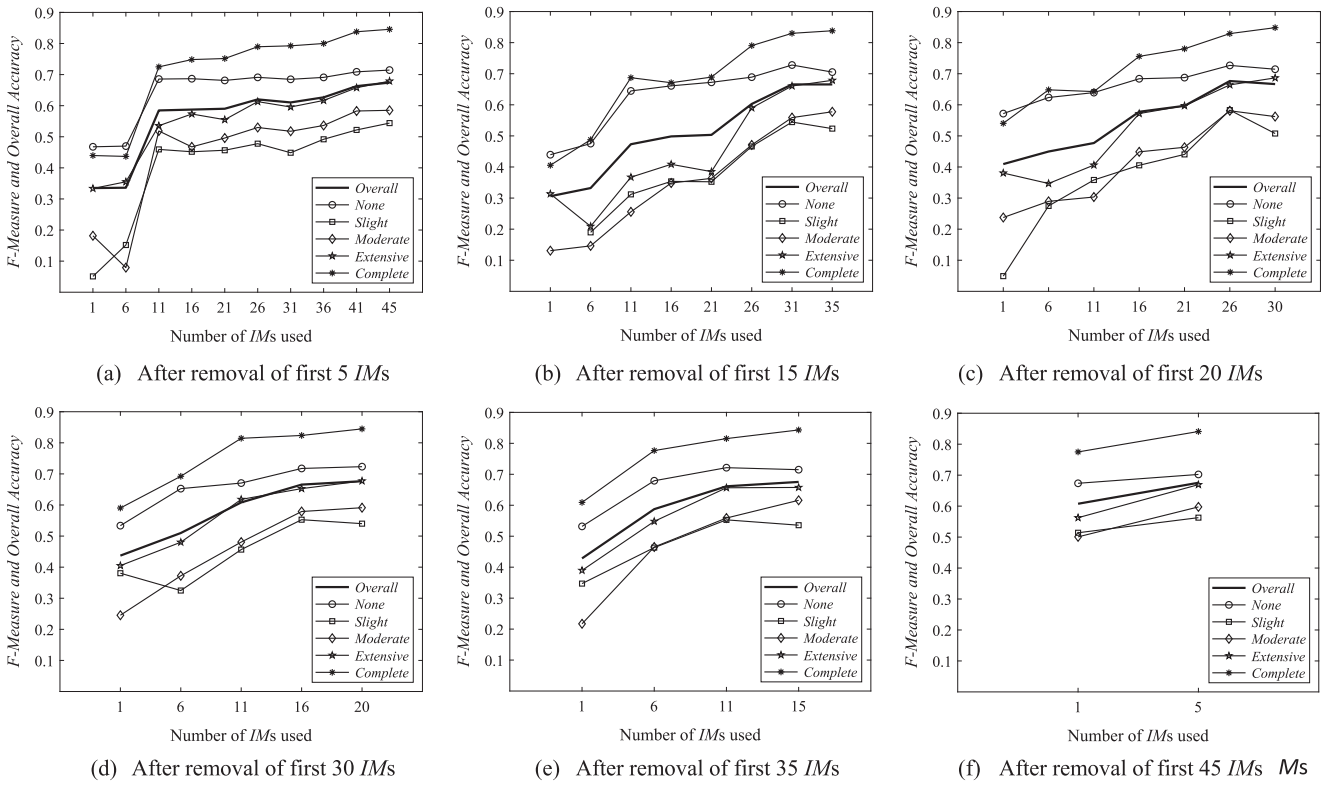

Fig. 8. *ANN* performance when less correlated *IM*s are gradually removed.

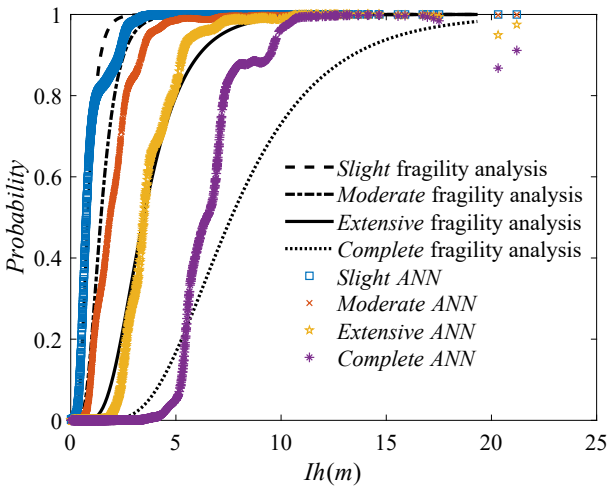

Fig. 9. Fragilty estimate comparison of the single-*IM ANN* classifier and Cloud method based on the same optimal *IM Ih*.

extraneous *IM*s which may compromise the *ANN* performance.

To further understand how the *IM* and *DR* correlation affects the *ANN* performance, the lower-ranking *IM*s are gradually removed. Fig. 8 shows that the overall accuracy with the initial single *IM* in (a)-(f) is 33.4%, 30.6%, 40.9%, 43.7%, 42.8%, and 60.8%, respectively. The overall increase of accuracy shows that higher-ranking *IM*s tend to generate better *ANN* performance, indicating the correlation ranking of *IM*s can provide a good guideline of *IM* selection for *ANN* seismic classifiers. Moreover, Fig. 8 coincides with the observations and discussions in Fig. 7.

4.3. ANN classifier vs. traditional fragility analysis

When predicting the global damage state of the benchmark building caused by a ground motion record, the activation softmax function $\sigma_3(\bullet)$ defined in Equation (6) of the *ANN* output layer generates the probability for each damage state based on the input *IM*s. For example, if the input *IM*s of a ground motion record lead to a damage probability vector of [0.001, 0.123, 0.638, 0.236, 0.002] via the *ANN* classifier, it means the probability $p[DR < 0.0033|\text{input } IMs]$ of this ground motion record resulting a *None* damage state is 0.001, and so on. Thus, we know the probability $p[DR \geq 0.0033|\text{input } IMs]$ is equal to 1–0.001 = 0.999, $p[DR \geq 0.0067|\text{input } IMs] = 1–0.001–0.123 = 0.876$, $p[DR \geq 0.02|\text{input } IMs] = 1–0.001–0.123–0.638 = 0.238$, $p[DR \geq 0.0533|\text{input } IMs] = 1–0.001–0.123–0.638–0.236 = 0.002$. These fragility estimates generated by the *ANN* seismic classifier are compared with the fragility estimates of Cloud method. Based on the same training and test datasets, Fig. 9 shows the fragility estimates obtained from a single-*IM ANN* classifier and the Cloud method with the same optimal *IM Ih*. The Cloud method may smooth out the details of damage state information as observed in [67]. Unlike the smooth traditional fragility curves, the fragility estimates obtained from *ANN* classifiers fluctuate as the *IM* increases. This fluctuation might be caused by the so-called "weaving" interaction observed in IDA curves [7], where a stronger ground motion may result in a lower absolute peak response and a lower fragility estimate due to earlier yielding. Thus, the seismic fragility estimates by *ANN* seismic classifiers might reflect this "weaving" interaction of scaled records while traditional fragility curves smooth out this detail. However, more studies like a direct comparison between the IDA method and the *ANN* classifier needs to be conducted in the future to validate this explanation. Besides, it is noticed that the discrepancy between fragility estimates by *ANN* classifiers and the fragility curves increases with higher *IM* values. As explained previously, the shape of Cloud fragility curves is governed by two parameters, i.e., the mean structural response and the standard deviation estimated by Equations (1) and (2), respectively. However, these two Equations could be false in the range of high

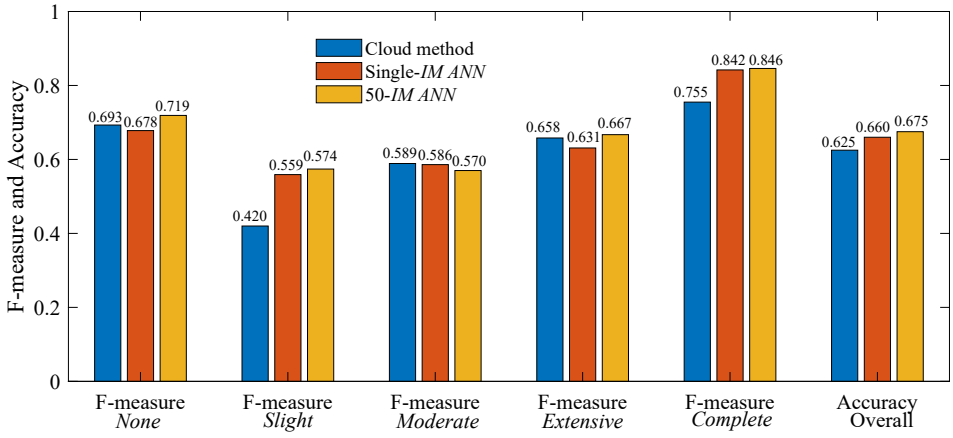

Fig. 10. The F-measure and overall accuracy of the Cloud method and single-*IM ANN* classifier both using the most correlated *IM, Ih*, and the multi-*IM ANN* classifier based on the same test dataset.

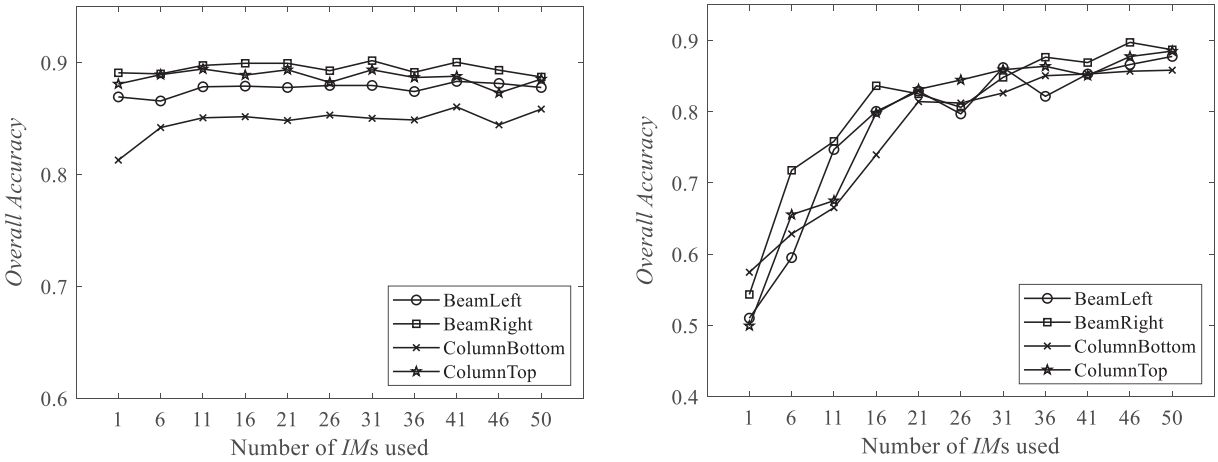

Fig. 11. Element-level *ANN* classification performance based on different subsets of *IMs*: (a) *IM* subsets selected in the most to least correlation order; (b) *IM* subsets selected in the least to most correlation order.

IMs, as proved in [7]. Thus, in the range of higher *IM* values that tend to cause the *Complete* damage to structures, the difference of fragility estimates between the *ANN* method and the Cloud method increases. This phenomenon is also observed in the non-parametric fragility curves in [67].

To further compare the *ANN* and Cloud approach, we generate the classification results of the same test dataset based on the fragility estimates obtained from the previous 50-*IM ANN* classifier, the single-*IM* classifier, and single-*IM* Cloud method. Their F-measure for each damage state and overall accuracy are compared in Fig. 10. The 50-*IM* ANN classifier outperforms the single-*IM* classifier and the Cloud method in terms of the overall accuracy and F-measure of all damage states except the *Moderate*. Particularly, the overall accuracy of the 50-*IM ANN* classifier is 67.5%, which is 5% higher than 62.5% of the Cloud method. These results demonstrate the superiority of directly mapping multiple *IMs* to the fragility estimates via the multivariate *ANN* seismic classifier.

5. Element-level multivariate *ANN* classifier

For post-event decision making of responses and repairs, additional knowledge of the local damage states of structural elements such as beams and columns is desired. The 72 element-level multivariate *ANN* classifiers for the two ends of 16 beams and 20 columns of the benchmark building are trained in the same way with the system-level *ANN* classifier. The plastic hinges formed at the ends of beams and columns are considered as important indicators of the seismic-induced local damage in frame structures [68]. In this study, the plastic hinge size at the ends of beams and columns is categorized into three states: *Small*, *Medium*, and *Large* based on a ductility μ of the outmost rebar of the cross section of beams and columns. The strain ductility μ is calculated by dividing the peak rebar strain with the steel yield strain of 0.00207. A plastic hinge is considered as *Small* when $\mu < 5$, *Medium* when $5 \leq \mu < 15$, and *Large* when $15 \leq \mu$ [69–71]. Take one side floorbeam on the second floor (Level 2) and one exterior column between the third (Level 3) and fourth floor (Level 4) as examples. For the four ends of the beam and column, denoted as BeamLeft, BeamRight, ColumnBottom, and ColumnTop in Fig. 12 (a), four element-level *ANN* classifiers are trained and tested using the previous 4,330 records. Their overall accuracy performance is presented in Fig. 11. Like the system-level *ANN* classifier, the number of selected *IMs* does not make a big difference to the *ANN* performance when the most correlated *IM* is included. Unlike the system-level classifier, the six least correlated *IMs* together may not provide highly accurate prediction of damage states. When the 21 less important *IMs* are included, the four element-level classifiers can achieve an overall accuracy of 80%-82%, which is close to 86%-89% of the 50 *IMs*. Despite the slightly different observation than the previous system-level *ANN* seismic classifier, the *IM* selection approach previously concluded for training multivariate *ANN* classifiers generally

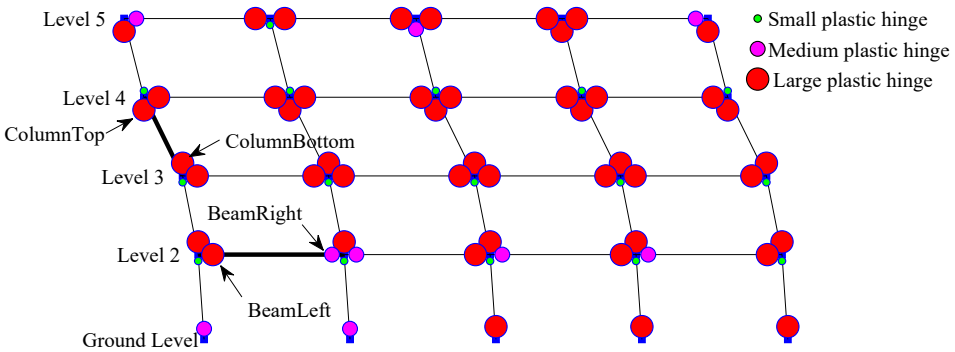

(a) Local damage distribution from the *NLTHA*

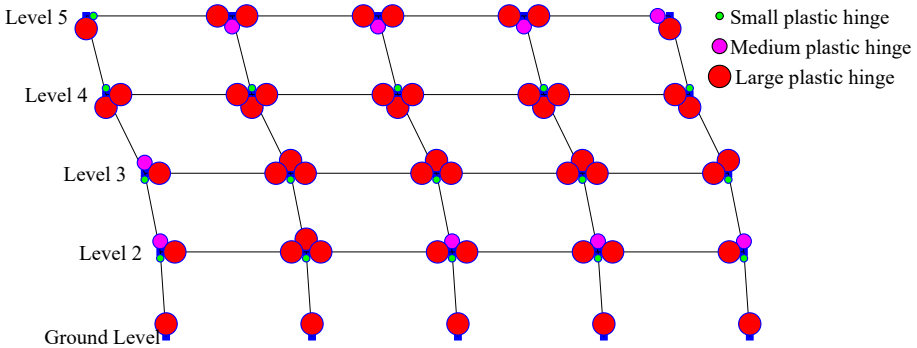

(b) Local damage distribution from the 72 *ANN* classifiers

Fig. 12. Local damage distribution of the perimeter frame under a synthesized Chi-Chi Earthquake ground motion: (a) local damage distribution from the *NLTHA*; (b) local damage distribution from the 72 *ANN* classifiers.

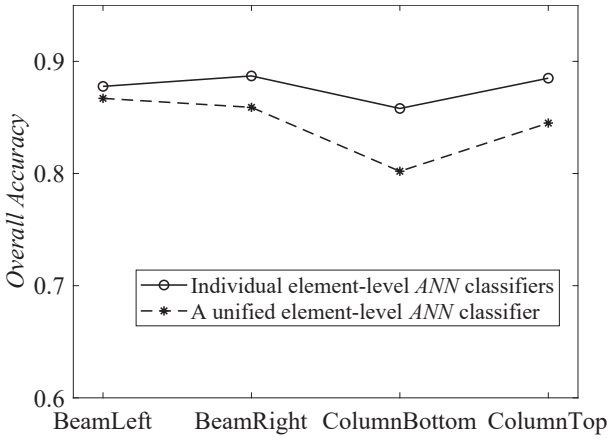

Fig. 13. Overall accuracy comparison between the unified element-level *ANN* classifier and the four individual element-level *ANN* classifiers.

applies to the elemental-level *ANN* classifiers.

To understand the distribution of plastic hinges in the benchmark building and further validate the *ANN* performance, the local structural damage map under a synthesized Chi-Chi Earthquake ground motion is obtained from the *NLTHA,* as presented in Fig. 12(a), and predicted by the trained 72 element-level *ANN* classifiers with 50 *IM*s, as shown in Fig. 12(b). Based on the *NLTHA*, the ground motion results in the *Complete* state to the perimeter frame with the peak interstory *DR* occurring between Level 3 and Level 4, which is consistent with the local damage distribution in Fig. 11(a). Specifically, five columns between Level 3 and Level 4 experience large plastic hinges at both ends while columns at other levels still have at least one small plastic hinge. Therefore, the story between Level 3 and Level 4 experiences the peak interstory drift based on the local damage distribution. Most beams are found to form large plastic hinges at both ends, which indicates more severe damage to the beams than columns because the perimeter frame was designed under the strong-column weak-beam provisions [46,72]. By comparing Fig. 12(b) with Fig. 12(a), the number of large hinges (17 in columns and 30 in beams) identified by the 72 element-level *ANN* classifiers is very close to the number of the large hinges (21 in columns and 26 in beams) obtained from *NLTHA*. The comparison shows that the *ANN* results can provide insightful information for the damage locations at the ends of beams and columns. The local element damage classification from the 72 *ANN* classifiers also identifies the peak interstory drift between Level 3 and Level 4. Therefore, the element-level *ANN* classifiers can complement the system-level *ANN* classifier for post-event damage evaluation.

Although the 72 individual element-level *ANN* seismic classifiers achieve good performance in the damage assessment of beams and columns of the frame structure, it is desirable in engineering practice to develop a unified element-level *ANN* classifier for the prediction of damage states in all elements. In this case, the input layer of the unified *ANN* classifier includes three neurons in addition to the *IM*s as illustrated in Fig. 1: two Cartesian coordinates relative to the left bottom column end as a reference origin to account for the location of each element end, and an integer to represent the end type of the element. The left and right ends of each beam are labeled as 1 and 2, respectively. The bottom and top ends of each column are 3 and 4, respectively. Fig. 13 compares

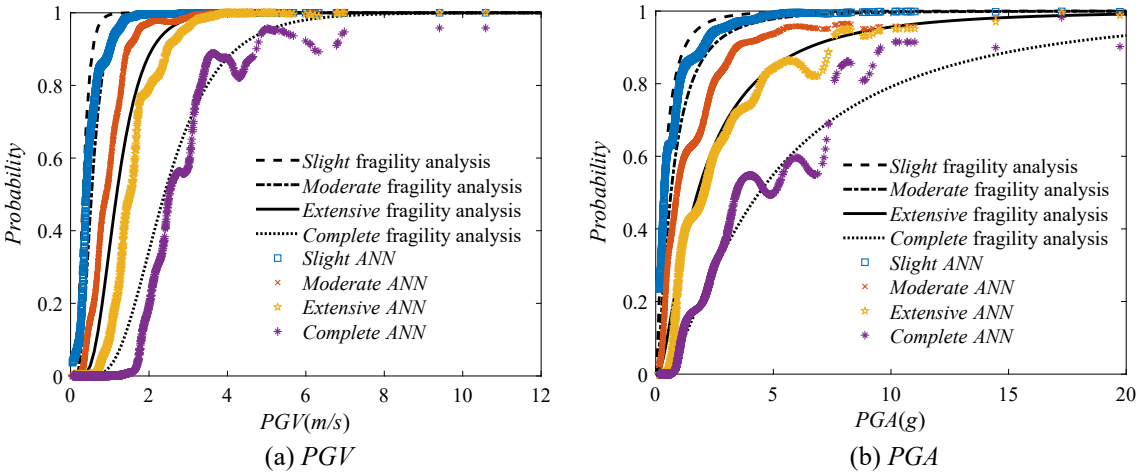

Fig. 14. Fragility estimate comparison of single-*IM ANN* approach and traditional fragility curves with: (a) *PGV*; (b) *PGA*.

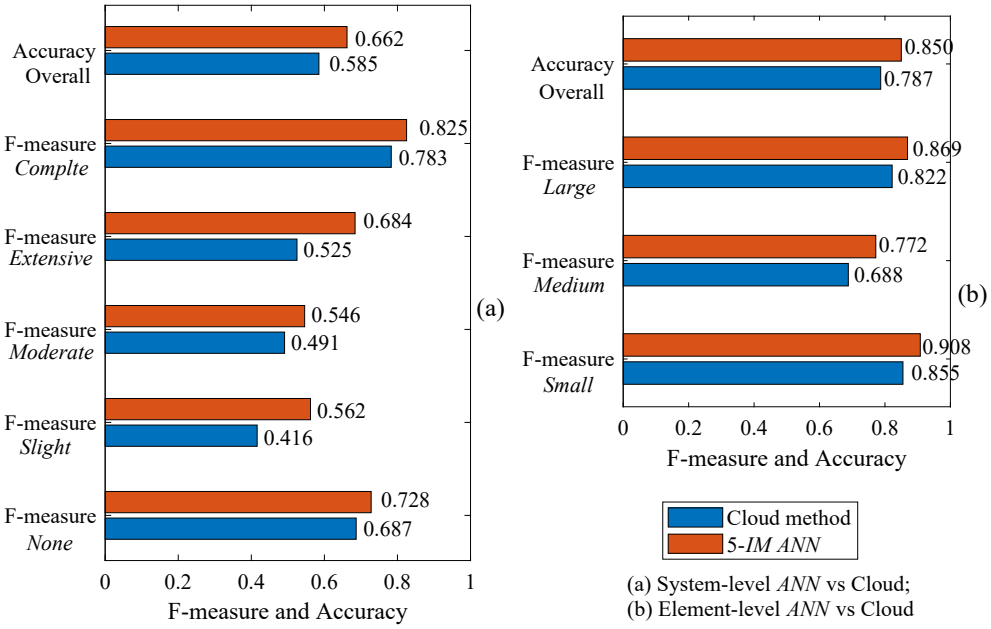

Fig. 15. The F-measure and overall accuracy comparison of Cloud method using the most correlated *PGV* and 5-*IM ANN* classifier based on the same test dataset: (a) system-level *ANN* versus Cloud; (b) element-level *ANN* versus Cloud.

the overall prediction accuracies between the unified element-level *ANN* classifier and the four individual *ANN* classifiers as marked in Fig. 12(a). It can be seen from Fig. 13 that, although slightly lower than that of the four individual classifiers, the overall accuracy of the unified classifier remains over 80%. The unified classifier thus has a satisfactory generalization ability for 72 element ends while it significantly reduces training and prediction time in practical applications.

6. Practical considerations

6.1. Readily available IMs

Readily available *IM*s are desired in engineering application [1]. Since the ShakeMap [35] can update five *IM*s in near real time in the wake of an earthquake event, an attempt is made to associate the proposed multivariate *ANN* classier with the five readily available *IM*s from the ShakeMap: *PGV*, *Sa-1.0*, *Sa-3.0*, *Sa-0.3*, and *PGA* (listed in Table 2 and 3). The system-level and the BeamLeft element-level *ANN* seismic classifiers are retrained with these five *IM*s. According to Fig. 4, *PGV*, *Sa-1.0*, *Sa-3.0*, *Sa-0.3*, and *PGA* were ranked 4th, 5th, 14th, 23rd, and 26th, respectively. *PGV* is the most correlated *IM* to *DR* of the benchmark building while *PGA* is the least correlated. Fig. 14 compares the fragility estimates from the system-level single-*IM ANN* classifier to the traditional fragility curves with *PGV* and *PGA*, respectively. *PGA* appears to give a better agreement between the *ANN* approach and the fragility analysis for low-intensity induced damage while *PGV* is for high-intensity induced damage likely due to the velocity pulses in near-fault ground motions. Fig. 14 further validates the observation on the "weaving" interaction as observed in Fig. 9.

Fig. 15 compares the F-measure of each damage state and the overall accuracy of the *ANN* classifier and Cloud method, respectively. The Cloud method uses the most correlated *PGV* as the input *IM*. The accuracy of the 5-*IM ANN* classifier is 7.7% (system level) and 6.3% (element level) higher than the Cloud method. The two 5-*IM ANN* classifiers also outperform the corresponding Cloud method in terms of F-measure in each damage state. The superior classification performance of multi-*IM ANN* classifiers validates that multivariate *ANN* seismic classifiers can better predict the post-earthquake damage states than the single-*IM*

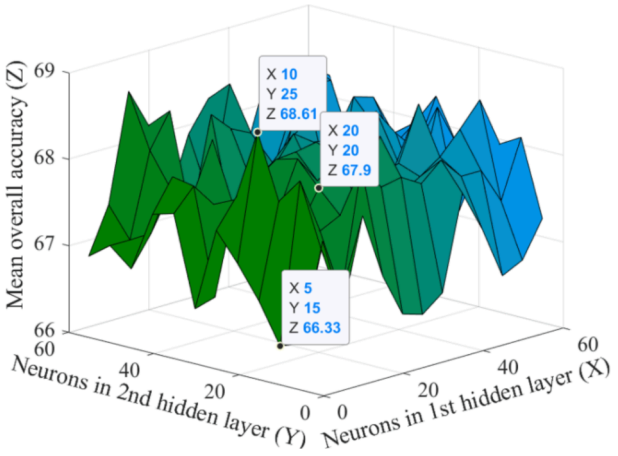

Fig. 16. The mean overall accuracy of the *ANN* models with different numbers of neurons in two hidden layers.

Cloud method.

6.2. Optimization of ANN configuration

As previously mentioned, this study configurated the *ANN* classifier with two hidden layers, each with 20 neurons, according to [36,37]. In engineering practice, however, an optimal configuration is desirable to achieve superior predictive performance. Although only a slight improvement on the overall accuracy seemed to have achieved when a second hidden layer was added into an *ANN* [34], an attempt was made to further investigate the optimal number of neurons in two hidden layers in this study. Specifically, the number of hidden neurons was selected to vary from 5 to 60 with an interval of 5. To ensure the generalizability of *ANN* models on unseen data in practice, the multifold cross-validation scheme [37] was adopted to train the *ANN* classifiers with the five readily available *IM*s as inputs. The collected samples were approximately divided evenly into K folds, one of which was used as unseen data for validation and the remaining K-1 folds were used for *ANN* training. The fold as unseen data for validation was rotated until all the folds have been chosen once so that the predictive model would be tested by the whole samples to guarantee its generalizability. The multifold cross-validation scheme degenerates into the leave-one-out (LOO) method when each fold contains one sample only. In this study, we divided the 4,330 samples into 10 folds, each having 433 samples. The mean value of the 10 overall accuracies in all 10 rotations was used to evaluate the *ANN* performance. Fig. 16 shows the mean overall accuracies of the *ANN* models with a different combination of neuron numbers in the two hidden layers. It can be seen form Fig. 16 that the *ANN* model with 10 and 25 neurons in the first and second hidden layers, respectively, achieves the highest mean overall accuracy of 68.61%. The *ANN* model with 5 and 15 neurons in the first and second hidden layers, respectively, achieves the lowest mean overall accuracy of 66.33%. Therefore, the improvement of the *ANN* accuracy by changing the number of neurons in hidden layers is relatively small. In fact, Fig. 16 clearly indicates many local maxima and local minima in the range of neuron numbers considered. There is no obvious global optimal accuracy observed in Fig. 16. The neuron numbers (10, 25) should not be regarded as a conclusive result for the optimal *ANN* architecture since no direct method is available to determine the optimal number of hidden neurons [34]. Instead, the trial-and-error method could be used to select the number of hidden neurons, as illustrated in Fig. 16.

6.3. Near real-time prediction

The computational efficiency is also an important factor in practical application. The training time of the 5-*IM ANN* seismic classifier is around 0.6 s with prepared training dataset while the test time of the 1,830 ground motion records is around 0.5 s, 0.27 ms per ground motion record in average. The *ANN* training and test are completed on the MATLAB platform in a regular PC with Intel (R) Core (TM) i5-2400 CPU @3.10 GHz (4 processors totally) and 8G RAM space. Once an *ANN* seismic classifier is well trained with the five ShakeMap *IM*s which will be updated near real time after an earthquake event, the saved *ANN* seismic classifier of the benchmark building can generate the fragility estimates and corresponding damage classification within 0.3 ms, which is near real time. This multivariate *ANN* seismic classifier can be used in conjunction with previously mentioned multi-parameter *ANN* seismic demand models [30,31]. The multi-parameter *ANN* seismic demand model can generate huge training data for the multivariate *ANN* seismic classifier in a short time without *NLTHA*. Thus, the performance of the multivariate *ANN* seismic classifier can be improved with more training data. The multivariate *ANN* seismic classifier can be incorporated in the framework of seismic fragility analysis and post-event damage evaluation as a promising tool.

7. Conclusions

The multivariate *ANN* seismic classifier is proposed to utilize multiple *IM*s as inputs for simultaneous seismic fragility estimation and damage classification. The system-level *ANN* classifier of a code-conforming benchmark building was trained to predict the global damage state measured by the maximum interstory drift ratio. As companions to the system-level *ANN* classifier, the element-level classifiers of the benchmark building were trained for the local damage classification of beams and columns and validate the global damage classification. Using the same test dataset, the multi-*IM ANN* seismic classifiers are 5% to 7.7% more accurate in overall classification than the single-*IM* fragility curves by Cloud method. The unified *ANN* classifier for all elements can be trained to satisfactorily predict the element-level fragility and damage state. By means of the multivariate *ANN* seismic classifier, the intensity and variety of earthquakes can be sufficiently considered without dealing with the mathematical difficulties of traditional multi-parameter regression approaches.

The *ANN* performance with different *IM* selections based on correlation ranking and model performance is investigated. Generally, more *IM*s which are highly correlated with the seismic structural responses will improve the *ANN* performance while redundant irrelevant *IM*s will compromise the performance. The optimal number of *IM*s that generates the best performance will vary with the classification targets like the system-level and element-level damage states. To select the optimal *IM* set, all *IM* candidates can be first ranked based on their correlation scores and then different *IM* combinations based on their ranking order (e.g., from the highest to lowest) can be experimented to select the optimal *IM* subset. Moreover, studies of *IM* selection show that even a few of the least correlated *IM*s, (6 for the system-level *ANN* classifier and 21 for the element-level *ANN* classifier) can achieve steady and high predictive performance, enabling more flexibility of *IM* selection in engineering practicality when the most correlated *IM*s are unknown or hard to access.

In practical considerations, first, five *IM*s (*PGV*, *PGA*, *Sa-1.0*, *Sa-3.0*, and *Sa-0.3*) readily available from the *USGS* ShakeMap are used as input to the multivariate *ANN* seismic classifiers, which achieve higher performance in both system level and element level than the traditional fragility curves by Cloud method. Second, an optimization of the *ANN* configuration classifier with the five readily available *IM*s is conducted by means of the 10-fold cross-validation. It shows that the *ANN* performance can be minorly improved with optimum configured networks. What's more, such a trained 5-*IM*s *ANN* classifier can generate the fragility estimates and damage state of a future ground motion record on the benchmark building in near real time (0.3 ms) using a general-purpose computer. Thus, the multivariate *ANN* seismic classifier can

be a promising tool for seismic fragility estimation and post-event damage classification in the wake of an earthquake.

The architecture and methodology of the proposed multivariate *ANN* seismic classifier is applicable to all types of buildings. Future studies can be directed to account for the effect of building configuration and geometry as part of the input to the multivariate *ANN* seismic classifier for simultaneous seismic fragility estimation and damage classification so that a well-trained classifier can be applied to estimate the distribution of damage states in an earthquake-stroke region. In addition, future studies of site-specific historic earthquakes are more realistic for *ANN* training than scaling historical ground motion records worldwide. It is also worthy to introduce methods like Small Sample Learning (SSL) to the multivariate *ANN* seismic classifiers, to reduce the computational efforts in this study which requires a large set of records for training.

CRediT authorship contribution statement

Xinzhe Yuan: Conceptualization, Data curation, Formal analysis, Investigation, Visualization, Methodology, Writing – original draft, Writing – review & editing. **Genda Chen:** Formal analysis, Investigation, Methodology, Writing – original draft, Writing – review & editing, Funding acquisition, Supervision. **Pu Jiao:** Data curation, Visualization, Writing – review & editing. **Liujun Li:** Methodology, Writing – review & editing. **Jun Han:** Data curation, Visualization. **Haibin Zhang:** Visualization.

Declaration of Competing Interest

The authors declare that they have no known competing financial interests or personal relationships that could have appeared to influence the work reported in this paper.

Acknowledgement

Financial support to complete this study was provided in part by the U.S. Department of Transportation, Office of Assistant Secretary for Research and Technology under the auspices of Mid-America Transportation Center at the University of Nebraska, Lincoln (grant no. 00072738). The reviews and comments by anonymous reviewers are highly appreciated.

References

[1] Padgett JE, Nielson BG, DesRoches R. Selection of optimal intensity measures in probabilistic seismic demand models of highway bridge portfolios. Earthq Eng Struct Dyn 2008;37(5):711–25. https://doi.org/10.1002/eqe.782.
[2] Kwon O-S, Elnashai A. The effect of material and ground motion uncertainty on the seismic vulnerability curves of RC structure. Eng Struct 2006;28(2):289–303. https://doi.org/10.1016/j.engstruct.2005.07.010.
[3] Padgett JE, DesRoches R. Sensitivity of seismic response and fragility to parameter uncertainty. J Struct Eng 2007;133(12):1710–8.
[4] Xie Y, Ebad Sichani M, Padgett JE, DesRoches R. The promise of implementing machine learning in earthquake engineering: a state-of-the-art review. Earthq Spectra 2020;36(4):1769–801. https://doi.org/10.1177/8755293020919419.
[5] Xie Y, Zhang J. Design and optimization of seismic isolation and damping devices for highway bridges based on probabilistic repair cost ratio. J Struct Eng 2018;144(8):04018125.
[6] Cornell CA, Jalayer F, Hamburger RO, Foutch DA. Probabilistic basis for 2000 sac federal emergency management agency steel moment frame guidelines. J Struct Eng 2002. doi: 10.1061/(asce)0733-9445(2002)128:4(526).
[7] Vamvatsikos D, Cornell CA. Incremental dynamic analysis. Earthq Eng Struct Dyn 2002;31(3):491–514. https://doi.org/10.1002/eqe.141.
[8] Jalayer F, Cornell CA. Alternative non-linear demand estimation methods for probability-based seismic assessments. Earthq Eng Struct Dyn 2009;38(8):951–72. https://doi.org/10.1002/eqe.876.
[9] Jalayer F, Ebrahimian H, Miano A, Manfredi G, Sezen H. Analytical fragility assessment using unscaled ground motion records. Earthq Eng Struct Dyn 2017;46(15):2639–63. https://doi.org/10.1002/eqe.2922.
[10] Miano A, Jalayer F, Ebrahimian H, Prota A. Cloud to IDA: efficient fragility assessment with limited scaling. Earthq Eng Struct Dyn 2018;47(5):1124–47. https://doi.org/10.1002/eqe.3009.
[11] Jalayer F, Elefante L, De Risi R, Manfredi G. Cloud analysis revisited: Efficient fragility calculation and uncertainty propagation using simple linear regression. In: NCEE 2014 - 10th U.S. natl. conf. earthq. eng. front. earthq. eng.; 2014. doi: 10.4231/D3SF2MC59.
[12] Jalayer F, De Risi R, Manfredi G. Bayesian Cloud Analysis: Efficient structural fragility assessment using linear regression. Bull Earthq Eng 2015;13(4):1183–203. https://doi.org/10.1007/s10518-014-9692-z.
[13] Celik OC, Ellingwood BR. Seismic fragilities for non-ductile reinforced concrete frames - role of aleatoric and epistemic uncertainties. Struct Saf 2010;32(1):1–12. https://doi.org/10.1016/j.strusafe.2009.04.003.
[14] Elefante L, Jalayer F, Iervolino I, Manfredi G. Disaggregation-based response weighting scheme for seismic risk assessment of structures. Soil Dyn Earthq Eng 2010;30(12):1513–27. https://doi.org/10.1016/j.soildyn.2010.07.003.
[15] Ellingwood BR, Celik OC, Kinali K. Fragility assessment of building structural systems in Mid-America. Earthq Eng Struct Dyn 2007;36(13):1935–52. https://doi.org/10.1002/eqe.693.
[16] Jeong S-H, Mwafy AM, Elnashai AS. Probabilistic seismic performance assessment of code-compliant multi-story RC buildings. Eng Struct 2012;34:527–37. https://doi.org/10.1016/j.engstruct.2011.10.019.
[17] Sasani M, Kiureghian AD. Seismic fragility of rc structural walls: Displacement approach. J Struct Eng 2001;127(2):219–28.
[18] Shinozuka M, Feng MQ, Lee J, Naganuma T. Statistical analysis of fragility curves. J Eng Mech 2000;126(12):1224–31.
[19] Baker JW. Probabilistic structural response assessment using vector-valued intensity measures. Earthq Eng Struct Dyn 2007;36(13):1861–83. https://doi.org/10.1002/eqe.700.
[20] Baker JW, Allin Cornell C. A vector-valued ground motion intensity measure consisting of spectral acceleration and epsilon. Earthq Eng Struct Dyn 2005;34(10):1193–217. https://doi.org/10.1002/eqe.474.
[21] Li Z, Li Y, Li N. Vector-intensity measure based seismic vulnerability analysis of bridge structures. Earthq Eng Eng Vib 2014;13(4):695–705. https://doi.org/10.1007/s11803-014-0273-6.
[22] Vamvatsikos D, Cornell CA. Developing efficient scalar and vector intensity measures for IDA capacity estimation by incorporating elastic spectral shape information. Earthq Eng Struct Dyn 2005;34(13):1573–600. https://doi.org/10.1002/eqe.496.
[23] Pang Y, Zhou X, He W, Zhong J, Hui O. Uniform design–based gaussian process regression for data-driven rapid fragility assessment of bridges. J Struct Eng 2021;147(4):04021008. https://doi.org/10.1061/(ASCE)ST.1943-541X.0002953.
[24] Du A, Padgett JE, Shafieezadeh A. Influence of intensity measure selection on simulation-based regional seismic risk assessment. Earthq Spectra 2020;36(2):647–72. https://doi.org/10.1177/8755293019891717.
[25] Calabrese A, Lai CG. Fragility functions of blockwork wharves using artificial neural networks. Soil Dyn Earthq Eng 2013;52:88–102. https://doi.org/10.1016/j.soildyn.2013.05.002.
[26] de Lautour OR, Omenzetter P. Prediction of seismic-induced structural damage using artificial neural networks. Eng Struct 2009;31(2):600–6. https://doi.org/10.1016/j.engstruct.2008.11.010.
[27] Lagaros ND, Fragiadakis M. Fragility assessment of steel frames using neural networks. Earthq Spectra 2007;23(4):735–52. https://doi.org/10.1193/1.2798241.
[28] Liu Z, Zhang Z. Artificial neural network based method for seismic fragility analysis of steel frames. KSCE J Civ Eng 2018;22(2):708–17. https://doi.org/10.1007/s12205-017-1329-8.
[29] Mitropoulou CC, Papadrakakis M. Developing fragility curves based on neural network IDA predictions. Eng Struct 2011;33(12):3409–21. https://doi.org/10.1016/j.engstruct.2011.07.005.
[30] Pang Y, Dang X, Yuan W. An artificial neural network based method for seismic fragility analysis of highway bridges. Adv Struct Eng 2014;17(3):413–28. https://doi.org/10.1260/1369-4332.17.3.413.
[31] Wang Z, Pedroni N, Zentner I, Zio E. Seismic fragility analysis with artificial neural networks: Application to nuclear power plant equipment. Eng Struct 2018;162:213–25. https://doi.org/10.1016/j.engstruct.2018.02.024.
[32] Kostinakis K, Morfidis K. Application of artificial neural networks for the assessment of the seismic damage of buildings with irregular infills' distribution. Geotech. Geol. Earthq. Eng. 2020;48:291–306. doi: 10.1007/978-3-030-33532-8_23.
[33] Morfidis K, Kostinakis K. Comparative evaluation of MFP and RBF neural networks' ability for instant estimation of r/c buildings' seismic damage level. Eng Struct 2019;197:109436. https://doi.org/10.1016/j.engstruct.2019.109436.
[34] Morfidis K, Kostinakis K. Approaches to the rapid seismic damage prediction of r/c buildings using artificial neural networks. Eng Struct 2018;165:120–41. https://doi.org/10.1016/j.engstruct.2018.03.028.
[35] Wald DJ, Worden BC, Quitoriano V, Pankow KL. ShakeMap manual: technical manual, user's guide, and software guide; 2006.
[36] Sontag ED. Feedback stabilization using two-hidden-layer nets. IEEE Trans Neural Networks 1992;3(6):981–90. https://doi.org/10.1109/72.165599.
[37] Haykin S. Neural networks and learning machines. 2008. doi: 978-0131471399.
[38] Hazus. Hazus–MH 2.1: technical manual. Fed Emerg Manag Agency 2012.
[39] Nair V, Hinton GE. Rectified linear units improve Restricted Boltzmann machines. In: ICML 2010 - Proceedings, 27th int. conf. mach. learn., 2010.
[40] Bridle JS. Probabilistic interpretation of feedforward classification network outputs, with relationships to statistical pattern recognition. Neurocomputing 1990. doi: 10.1007/978-3-642-76153-9_28.
[41] Bridle JS. Training stochastic model recognition algorithms as networks can lead to maximum mutual information estimation of parameters. Adv Neural Inf Process Syst 1990.

[42] Krizhevsky A, Sutskever I, Hinton GE. ImageNet classification with deep convolutional neural networks. Commun ACM 2017;60(6):84–90. https://doi.org/10.1145/3065386.
[43] Gao B, Pavel L. On the properties of the softmax function with application in game theory and reinforcement learning. ArXiv 2017.
[44] Pang T, Xu K, Dong Y, Du C, Chen N, Zhu J. Rethinking softmax cross-entropy loss for adversarial robustness. ArXiv 2019.
[45] Ruder S. An overview of gradient descent optimization algorithms. ArXiv Prepr ArXiv160904747 2016.
[46] Haselton CB, Goulet CA, Mitrani-Reiser J, Beck JL, Deierlein GG, Porter KA, et al. An assessment to benchmark the seismic performance of a code-conforming reinforced concrete moment-frame building. Peer Rep 2008.
[47] Spacone E, Filippou FC, Taucer FF. Fibre beam-column model for non-linear analysis of R/C frames: Part I. Formulation. Earthq Eng Struct Dyn 1996. https://doi.org/10.1002/(SICI)1096-9845(199607)25:7<711::AID-EQE576>3.0.CO;2-9.
[48] McKenna F. OpenSees: a framework for earthquake engineering simulation. Comput Sci Eng 2011;13(4):58–66. https://doi.org/10.1109/MCSE.2011.66.
[49] Luco N, Bazzurro P. Does amplitude scaling of ground motion records result in biased nonlinear structural drift responses? Earthq Eng Struct Dyn 2007;36(13):1813–35. https://doi.org/10.1002/eqe.695.
[50] Bazzurro P, Cornell CA, Shome N, Carballo JE. Three proposals for characterizing mdof nonlinear seismic response. J Struct Eng 1998;124(11):1281–9.
[51] Mackie KR, Stojadinovic B. Comparison of incremental dynamic, cloud, and stripe methods for computing probabilistic seismic demand models. Proc. Struct. Congr. Expo. 2005. https://doi.org/10.1061/40753(171)184.
[52] Billah AHMM, Alam MS, Bhuiyan MAR. Fragility analysis of retrofitted multicolumn bridge bent subjected to near-fault and far-field ground motion. J Bridg Eng 2013;18(10):992–1004.
[53] Mangalathu S, Heo G, Jeon J-S. Artificial neural network based multi-dimensional fragility development of skewed concrete bridge classes. Eng Struct 2018;162:166–76. https://doi.org/10.1016/j.engstruct.2018.01.053.
[54] Li Z, Kotronis P, Wu H. Simplified approaches for Arias Intensity correction of synthetic accelerograms. Bull Earthq Eng 2017;15(10):4067–87. https://doi.org/10.1007/s10518-017-0126-6.
[55] Zhong J, Jeon J-S, Shao Y-H, Chen L. Optimal intensity measures in probabilistic seismic demand models of cable-stayed bridges subjected to pulse-like ground motions. J Bridg Eng 2019;24(2):04018118. https://doi.org/10.1061/(ASCE)BE.1943-5592.0001329.
[56] Nielson BG. Analytical fragility curves for highway bridges in moderate seismic zones. 2005.
[57] Riddell R. On ground motion intensity indices. Earthq Spectra 2007;23(1):147–73. https://doi.org/10.1193/1.2424748.
[58] De Biasio M. Ground motion intensity measures for seismic probabilistic risk analysis. 2014.
[59] Elghazouli AY, Kumar M, Stafford PJ. Prediction and optimisation of seismic drift demands incorporating ground motion frequency content. Bull Earthq Eng 2014;12(1):255–76. https://doi.org/10.1007/s10518-013-9568-7.
[60] Kostinakis K, Athanatopoulou A, Morfidis K. Correlation between ground motion intensity measures and seismic damage of 3D R/C buildings. Eng Struct 2015;82:151–67. https://doi.org/10.1016/j.engstruct.2014.10.035.
[61] Rathje EM, Faraj F, Russell S, Bray JD. Empirical relationships for frequency content parameters of earthquake ground motions. Earthq Spectra 2004;20(1):119–44. https://doi.org/10.1193/1.1643356.
[62] Basheer IA, Hajmeer M. Artificial neural networks: fundamentals, computing, design, and application. J Microbiol Methods 2000;43(1):3–31. https://doi.org/10.1016/S0167-7012(00)00201-3.
[63] Hall MA, Smith LA. Feature selection for machine learning: comparing a correlation-based filter approach to the wrapper. In: FLAIRS conference, vol. 1999. p. 235–9.
[64] Møller MF. A scaled conjugate gradient algorithm for fast supervised learning. Neural Networks 1993;6(4):525–33. https://doi.org/10.1016/S0893-6080(05)80056-5.
[65] Demuth H, Beale M. Neural network toolbox - for use with MATLAB. 2002. doi: 10.1016/j.neunet.2005.10.002.
[66] Sasaki Y. The truth of the F-measure. Teach Tutor Mater 2007.
[67] Mai C, Konakli K, Sudret B. Seismic fragility curves for structures using non-parametric representations. Front Struct Civ Eng 2017;11(2):169–86. https://doi.org/10.1007/s11709-017-0385-y.
[68] Oinam RM, Sahoo DR, Sindhu R. Cyclic response of non-ductile rc frame with steel fibers at beam-column joints and plastic hinge regions. J Earthq Eng 2014;18(6):908–28. https://doi.org/10.1080/13632469.2014.916239.
[69] Brachmann I, Browning JA, Matamoros A. Drift-dependent confinement requirements for reinforced concrete columns under cyclic loading. ACI Struct J 2004. https://doi.org/10.14359/13389.
[70] Han J, Li YM, Ji SY. Realization of rational failure mechanism for the RC frame structure. Harbin Gongye Daxue Xuebao/Journal Harbin Inst Technol 2010.
[71] Han J, Du Y, Li Y, Liu L. Application of equivalent linearization method in design of RC frame structure. Jianzhu Jiegou Xuebao/Journal Build Struct 2016. https://doi.org/10.14006/j.jzjgxb.2016.05.021.
[72] American Concrete Institute - ACI Committee 318. Building code requirements for structural concrete (ACI 318S-05) and commentary (ACI 318SR-05); 2005. doi: 10.1016/S1130-6343(05)73662-X.